This is a preprint of the following article, which is available from mdolab.engin.umich.edu
S. Kaneko and J. R. R. A. Martins. Simultaneous Optimization of Conceptual Design and Takeoff Trajectory of a Lift-Plus-Cruise UAV. *10th Autonomous VTOL Technical Meeting*, Mesa, AZ, January 2023.
The original article may differ from this preprint and is available at
https://vtol.org/store/product/simultaneous-optimization-of-conceptual-design-and-takeoff-trajectory-of-a-liftpluscruise-evtol-uav-17770.cfm.

Simultaneous Optimization of Conceptual Design and Takeoff Trajectory of a Lift-Plus-Cruise UAV

Shugo Kaneko and Joaquim R. R. A. Martins
Department of Aerospace Engineering, University of Michigan, Ann Arbor, MI, 48109

Abstract

Vertical takeoff and landing (VTOL) aircraft design requires consideration of an efficiency trade-off between various flight conditions, including hover, transition, and cruise. To capture this trade-off, we propose simultaneous optimization of aircraft conceptual design and takeoff trajectory. Design-trajectory optimization, also called open-loop control co-design, allows us to find the optimal aircraft design that balances the flight efficiency between various flight conditions for maximum system-level performance. In this paper, we maximize the payload weight capacity of a lift-plus-cruise unmanned aerial vehicle (UAV) for package delivery. As a result, simultaneous optimization increases the payload weight by up to 5.3% compared to the conventional approach, which does not couple takeoff trajectory optimization to UAV conceptual design. We identify that the cruise speed and pusher motor sizing have a significant influence on takeoff trajectory. Simultaneous optimization finds the optimal cruise speed and motor sizing that enables energy-efficient wing-borne climb, which is not always possible with conventional sequential optimization.

Notation

AR	=	wing aspect ratio
C_D	=	drag coefficient
C_L	=	lift coefficient
c	=	rotor blade chord, m
D	=	drag, N
d	=	rotor-fuselage separation, m
E	=	energy, J
F	=	rotor in-plane force, N
g	=	gravity constant, m/s^2
L	=	lift, N
m	=	UAV total weight, kg
P	=	power consumption, W
$\bar{P}$	=	motor power rating, W
R	=	rotor radius, m
S	=	wing area, m^2
T	=	rotor thrust, N
t	=	time, s
v	=	velocity, m/s
W	=	component weight, kg
w	=	fuselage width, m
x	=	horizontal location, m
y	=	altitude, m
α	=	angle of attack, rad
θ	=	body pitch angle, rad
γ	=	flight path angle, rad
Ω	=	rotor rotational speed, rad/s
ϕ	=	rotor blade twist, rad
ρ_b	=	battery density, Wh/kg
$()_0$	=	initial condition
$()_f$	=	terminal condition

1 Introduction

The transportation of commercial packages and medical supplies is an essential application of unmanned aerial vehicles (UAVs). UAV delivery—also known as *drone delivery*—is faster and potentially more environmentally friendly than conventional ground delivery [1]. Vertical takeoff and landing (VTOL) configurations with a wing, such as a tailsitter and lift-plus-cruise, are viable for UAV delivery because the efficient wing-borne cruise enables a longer range compared to wingless multirotors. This work contributes to the conceptual design methodology of VTOL UAVs.

One of the main challenges in designing a VTOL aircraft is the diverse flight conditions, which vary from hover to wing-borne forward flight. In general, there is a trade-off between vertical flight efficiency and cruise efficiency: a cruise-efficient UAV design is not very efficient in vertical flights (i.e., hover, vertical climb, and descent), and vice versa. Therefore, we need to balance the two contradicting factors to design an efficient vehicle in terms of system-level performance (e.g., total energy consumption, payload weight capacity, and UAV total weight). One common approach is multipoint design optimization: for example, we maximize the weighted sum of the hover and cruise efficiency. The resulting design performs well (but not the best) in both vertical and cruise conditions. However, selecting an appropriate weighting factor for each flight condition of multipoint optimization is often difficult. Furthermore, this approach typically ignores transition performance, which is a mixture of vertical and cruise performance. Transition is more challenging to account for in the conceptual design process because of its inherently dynamic nature.

To address these challenges, we propose simultaneous optimization of the UAV conceptual design and takeoff flight trajectory to maximize system-level performance. In this work, we maximize the payload weight capacity of a package delivery lift-plus-cruise UAV given the mission requirements. The simultaneous optimization allows us to find the optimal balance of the UAV performance at various flight conditions, including the dynamic transition.

This paper is composed as follows. In Section 2, we briefly review the relevant literature. Section 3 explains the models of the UAV dynamics, aerodynamics, rotor analysis, and weight estimation we use in this study. Section 4 presents the problem formulation and result of simple UAV conceptual design optimization, which is not coupled to trajectory optimization. Then, Section 5 discusses takeoff trajectory optimization while fixing the vehicle design. In Section 6, we describe the novel simultaneous design-trajectory optimization problem. We also discuss the difference between the UAV designs obtained by the simultaneous optimization and the one from conventional sequential optimization.

2 Relevant Literature

Electric VTOL (eVTOL) UAV Conceptual Design. Modeling and Optimization of eVTOL UAV conceptual design have been an active research topic over the last decade. For the lift-plus-cruise configuration, Tyan et al. [2] presented a conceptual sizing study of a 3.5-kg UAV. Zhang et al. [3] optimized the design of a lift-plus-cruise UAV's electric propulsion system. An et al. [4] investigated a hydrogen-electric lift-plus-cruise UAV design. Chakraborty and Mishra [5] also presented a comprehensive sizing method for an electric lift-plus-cruise aircraft, although they studied urban air mobility (UAM) aircraft but not small UAVs. For the wingless multirotor configuration, Bershadsky et al. [6] presented regression models and performed conceptual design optimization. Winslow et al. [7] proposed component weight estimation models for quadrotor sizing. Vu et al. [8] also proposed electric propulsion system sizing models for multirotors. On the tailsitter, Sridharan et al. [9] investigated the quadrotor biplane tailsitter design of various vehicle sizes. The same authors also performed multidisciplinary design optimization (MDO) of the same

Table 1: Summary of recent VTOL trajectory optimization literature.

Authors	Year	Configuration	Takeoff weight, kg	Trajectory problem
Panish et al. [16]	2022	tiltwing	6.9	forward[1] and backward[2] transition
Orndorff et al. [13]	2022	lift-plus-cruise	3724.0	forward transition
Delbecq et al. [17]	2021	multirotor	50.8	vertical climb
Wang et al. [14]	2021	lift-plus-cruise	600.0	maneuverability assessment
Anderson et al. [15]	2021	tailsitter	1.4	takeoff and forward transition
Chauhan et al. [18]	2020	tiltwing	725.0	takeoff and forward transition
Pradeep et al. [19]	2018	tiltwing	752.0	backward transition and descent
Verling et al. [20]	2017	tailsitter	3.0	backward transition
Oosedo et al. [21]	2017	tailsitter	1.6	forward transition
Banazadeh et al. [22]	2016	tailsitter	46.0	forward and backward transition
Maqsood et al. [23]	2012	tiltwing	–	forward and backward transition
Kubo et al. [24]	2008	tailsitter	2.0	forward and backward transition

[1]Forward transition: hover-to-cruise [2]Backward transition: cruise-to-hover

tailsitter UAV [10]. There also exits the research to compare multiple configurations. Govindarajan and Sridharan [11] performed conceptual design optimization of multirotors, a tailsitter, and a tiltable tricopter for package delivery. Palaia et al. [12] discussed the comparison of different eVTOL configurations, although their work focused on UAM-scale aircraft.

eVTOL Trajectory Optimization. Orndorff and Hwang [13] performed trajectory optimization of a constant-altitude forward transition (i.e., hover-to-cruise transition) of a lift-plus-cruise air taxi. Wang et al. [14] used trajectory optimization to evaluate the maneuverability of a lift-plus-cruise aircraft for UAM. For lightweight UAVs, Anderson et al. [15] reported a comparison of the aerodynamic models for tailsitter trajectory optimization. Other trajectory optimization literature is summarized in Table 1. The table mostly focuses on the VTOL UAV trajectory optimization work, but it also includes a few relevant papers on the UAM application.

Simultaneous Design-Trajectory Optimization. In this paper, we combine the UAV conceptual design optimization and trajectory optimization into a monolithic optimization problem. The design-trajectory optimization is also called *open-loop control co-design* [25]. Allison et al. [26] summarized various problem formulations for co-design optimization and correlated the co-design formulations to the MDO architectures [27, 28]. Herber et al. [29] compared the nested and simultaneous optimization approaches for co-design. They also performed benchmark studies on a few test problems. On the application side, Delbecq et al. [17] performed design-trajectory optimization of a wingless multirotor. They optimized the UAV sizing variables and one-dimensional vertical climb trajectory. Other aerospace applications of design-trajectory optimization include the work on a fixed-wing UAV [30], a high altitude long endurance (HALE) aircraft [31], a hypersonic waverider [32], and a launch vehicle [33].

3 Models

3.1 UAV Configuration and Baseline Specification

We study a lift-plus-cruise eVTOL configuration in this paper. A lift-plus-cruise aircraft has two distinct sets of rotors, one for cruise thrust and the other for vertical lift. The lift-plus-cruise vehicles are efficient in both vertical flight and wing-borne cruise because each propulsion system is tailored independently to its operating conditions. The vertical propulsor is designed to be efficient in hover and vertical flights, whereas the cruise propulsor is designed for higher-speed forward flight conditions. Another advantage of the lift-plus-cruise configuration is mechanical simplicity, unlike

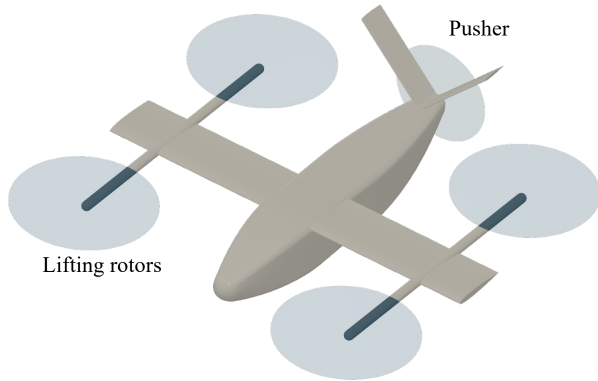

Figure 1: Lift-plus-cruise configuration.

Table 2: Baseline specification of the Wing's UAV [36].

Description	Value
Takeoff weight	6.4 kg
Payload weight	1.2 kg
Roundtrip range	20 km
Cruise speed	29 m/s
Cruise altitude	45 m
Wing span	1 m
Wing area	0.152 m^2

tiltwing or tiltrotor that require a complex tilt mechanism. This simplicity is particularly preferable for lightweight UAVs. The shortcomings are the additional weight and drag due to the redundant propulsion systems compared to tailsitters or vectored thrust aircraft, which use the same propulsor in both vertical flight and cruise.

Figure 1 shows a notional vehicle configuration we investigate in this work. The vehicle has one pusher and four lifting rotors attached to the wing via the booms. All lifting rotors are two-bladed, which is important to reduce the lifting rotor drag in the cruise. Aligning the blades parallel to the flow reduces the cruise drag significantly compared to placing the blades perpendicular to the flow [34]. We also use a two-blade propeller for the pusher because most of the off-the-shelf small-scale rotors have two blades [35].

In this paper, the mission setups and the baseline UAV specification are based on the Wing's package delivery UAV [36], as summarized in Table 2.

3.2 Vehicle Dynamics

We consider two-degree-of-freedom dynamics in the longitudinal plane. This dynamics model regards the body pitch angle as a control input. Figure 2 shows the schematic of vehicle dynamics.

The equations of motion are

$$\begin{aligned} m\dot{v_x} &= (T_{\text{pusher}} - F)\cos\theta - T_{\text{lifter}}\sin\theta - D\cos\gamma - L\sin\gamma \ , \\ m\dot{v_y} &= (T_{\text{pusher}} - F)\sin\theta - T_{\text{lifter}}\cos\theta - D\sin\gamma + L\cos\gamma - mg \ , \end{aligned} \tag{1}$$

where m is the vehicle mass, v_x and v_y are the horizontal and vertical speed, θ is the pitch angle relative to the horizontal plane, and γ is the flight path angle given by $\gamma = \arctan(v_x/v_y)$. L and D are the lift and drag. T_{pusher} and T_{lifter} are the thrust of the pushing rotor and lifting rotors,

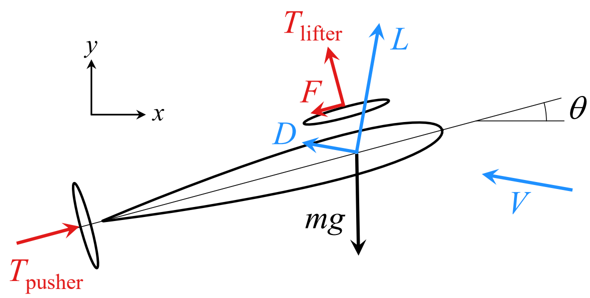

Figure 2: Dynamics model of a lift-plus-cruise UAV.

respectively. F is the in-plane force of the lifting rotor, which is non-zero when the inflow is not normal to the rotor disk, for example, edgewise forward flight. We ignore the pusher's in-plane force because the pusher inflow is nearly normal except for the vertical flights, where the inflow speed is low and the in-plane force is insignificant. In Eq. (1), m and g are time-independent, whereas all the other variables are a function of time.

In addition, an ordinal differential equation for energy consumption is

$$\dot{E}(t) = P(t) \ , \tag{2}$$

where E is accumulated energy consumption and P is the power required by the rotors.

The lift and drag are computed using a simple aerodynamic model, and the rotor thrusts and powers are computed using the blade element momentum (BEM) analysis:

$$\begin{aligned} L, D &= f_{\text{aero}}(v_x, v_y, \theta) \ , \\ T, F, P &= f_{\text{rotor}}(v_x, v_y, \theta, \Omega) \ , \end{aligned} \tag{3}$$

where Ω is the angular velocity control input of a rotor. We perform a rotor analysis for each of the pushing and lifting rotors because they have different rotor designs and control inputs.

3.3 Aerodynamic Model

The aerodynamic model computes the lift and drag coefficients as a function of the angle of attack α. VTOL trajectory analysis requires a post-stall aerodynamic model because the wing stalls in vertical and initial transition phases. We use an aerodynamic model used in the eVTOL trajectory optimization work by Ref. 18. This model combines airfoil's pre-stall data (C_L and C_D at various angles of attack), a finite-wing correction based on the lifting-line theory, and a post-stall model developed in Ref. 37. The pre-stall airfoil data in this study was generated using XFOIL [38] on NACA 0012 airfoil at $Re = 200,000$. We assumed a constant wing aspect ratio of 6.6, which is the estimated aspect ratio of the Wing's UAV, and the Oswald efficiency of 0.8.

Lift-plus-cruise eVTOLs suffer from a higher drag coefficient in cruise than conventional fixed-wing aircraft because of the additional drag from the lifting rotors. We use the minimum C_D of 0.0397 based on Ref. 34, who performed wind-tunnel experiments of a lift-plus-cruise configuration at a similar Reynolds number to our study. We then adjusted the $C_D - \alpha$ curve from the above aerodynamic model to yield $C_{D_{\min}} = 0.0397$. The resulting lift and drag coefficient models are shown in Fig. 3.

3.4 Rotor Analysis

We use the blade element momentum (BEM) theory for rotor analysis. The BEM model computes the rotor thrust, in-plane force, and power given the rotor rotational speed, inflow speed,

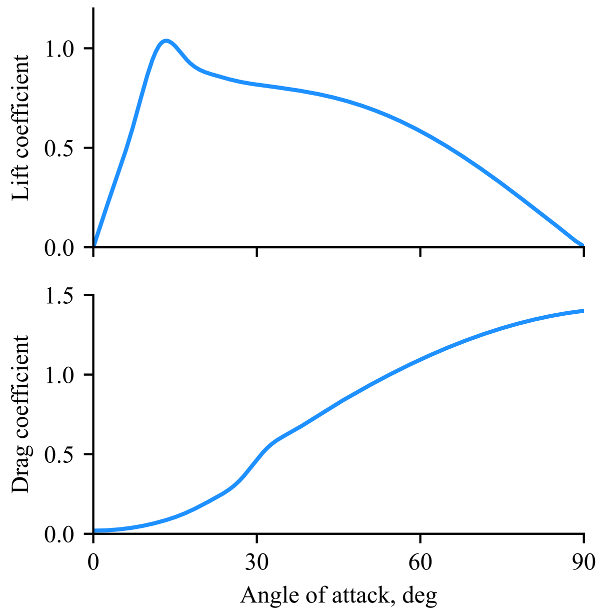

Figure 3: Lift and drag coefficient models.

and inflow angle with respect to the rotor disk plane. Then, the thrust and in-plane force are used in Eq. (1), and the power is integrated to compute the energy consumption by Eq. (2).

We use CCBlade [39] as a BEM implementation. This package is implemented in Julia, and we use a Julia wrapper[1] to call CCBlade within the OpenMDAO framework [40], on which all the other models are implemented. We used the Prandtl correction for the tip and hub loss. The hub diameter is assumed to be 15% of the rotor diameter, which is the typical value of off-the-shelf small rotors [8, 35].

To compute the power required, we assume a constant motor efficiency of 0.95 [5]. We also estimate the loss due to the boom-rotor interaction using a simple geometry-based model [5, 41]. The baseline geometry gives a factor of 0.97, and we use this factor throughout the optimization. The pusher-body interaction is ignored.

3.5 Weight Estimation

The component weights of the wing, rotors, motors, electric speed controllers (ESCs), and battery are estimated using the following models [6, 11, 42]:

$$W_{\text{wing}} = -0.0802 + 2.2854S \ , \tag{4}$$

$$W_{\text{rotor}} = 0.7484R^2 - 0.0403R \ , \tag{5}$$

$$W_{\text{motor+ESC}} = 6.1 \times 10^{-4}\bar{P} \ , \tag{6}$$

$$W_{\text{battery}} = \frac{E_{\text{total}}}{(0.85 \times 0.8)\rho_b} \ , \tag{7}$$

where S is the wing area, R is the rotor radius, and $\bar{P}$ is the motor power rating. Eqs. (4)–(6) uses the SI units. The battery weight is determined based on the energy required for a round-trip mission E_{total} and the energy density ρ_b. We use a battery density of 158 Wh/kg, which includes the additional weight of the casing [11]. In Eq. (7), the factor of 0.85 accounts for the losses

[1] https://github.com/byuflowlab/OpenMDAO.jl.

Table 3: UAV static design optimization problem.

		Function/variable	Description
maximize		W_{payload}	payload weight capacity
by varying	design	S	wing area
		v_{cruise}	cruise speed
		$\bar{P}_{\text{lifter}}$, $\bar{P}_{\text{pusher}}$	power rating of lifting motors and a pushing motor
		R_{lifter}, R_{pusher}	radius of lifting and pushing rotors
		ϕ_{lifter}, ϕ_{pusher}	blade twist distribution of each rotor set
		c_{lifter}, c_{pusher}	blade chord distribution of each rotor set
	control	θ	body pitch attitude at each flight conditions
		Ω_{lifter}, Ω_{pusher}	rotor speed at each flight conditions
		$v_{x,\text{climb}}$	horizontal speed at climb point
subject to	design	$C_L \leq 0.8$	lift coefficient in cruise
		$P_{\text{hover-out}} \leq \bar{P}_{\text{lifter}}$	power constraint at one-motor-out hover point
		$P_{\text{climb}} \leq \bar{P}_{\text{pusher}}$	power constraint at climb point
		$v_x \leq 100$ (mph)	speed limit in cruise and climb points (FAA Part 107)
		$g(r_{\text{lifter}}, S) \leq 0$	spanwise geometry constraint
		$c \leq 0.35r$	rotor chord upper bounds
	trim	$\dot{v_y} = 0$	vertical equilibrium at each flight condition
		$\dot{v_x} = 0$	horizontal equilibrium at each flight condition

in transmission and onboard system powers [9], and 0.8 is to secure the reserve energy, which is assumed to be 20% of the mission energy [43].

Then, the payload weight is given by

$$W_{\text{payload}} = W_{\text{total}} - (W_{\text{rotor}} + W_{\text{motor+ESC}} + W_{\text{wing}} + W_{\text{battery}} + W_{\text{others}}) \,, \tag{8}$$

where W_{total} is the total takeoff weight, and W_{others} are the weight of all the other items, including fuselage structure, avionic, and wiring. The total weight and misc weight are fixed during optimization in this study. To estimate the miscellaneous weight W_{others}, we set the payload weight of the statically-optimized design (explained in Sec. 4) to 1.2 kg, which is the maximum payload capacity of the Wing's UAV. We then estimate W_{others} in a reverse manner by subtracting the component weights from the fixed total weight (6.4 kg) following Eq. (8). This gives $W_{\text{others}} = 3.859$ kg.

4 UAV Static Design Optimization

The first optimization problem maximizes the payload weight capacity while fixing the total takeoff weight. We call this problem *static* because it does not include the trajectory analysis and is based only on steady flight conditions. The UAV design variables are the wing area, cruise speed, motor power ratings, rotor radius, and the chord and twist distribution of rotor blades. The chord and twist distribution is parametrized by b-splines with 5 spanwise control points. We independently design the lifting propulsor (motors and rotors) and the pushing propulsor. In addition, the component weights of the payload, battery, motors, ECSs, rotors, and wing also vary following Eqs. (4)–(8), although these parameters are not independent optimization variables. The static design optimization problem is summarized in Table 3.

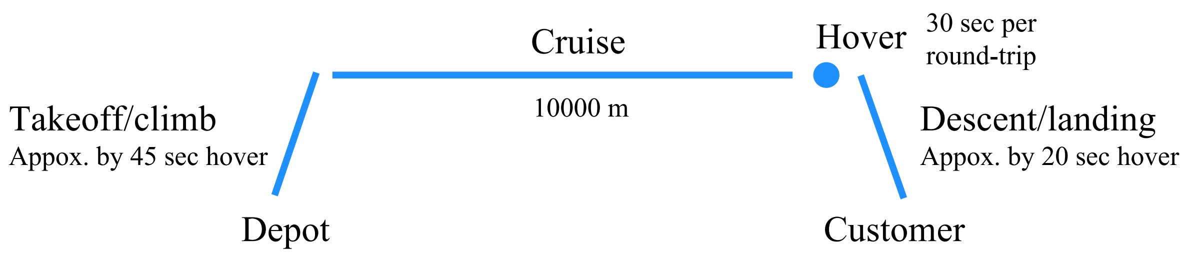

Figure 4: Mission profile used to compute the total energy consumption in static design optimization. The figure only shows a one-way flight; in optimization, we compute the energy for a round-trip flight.

4.1 Steady Flight Conditions

The static optimization formulation includes four steady flight conditions: cruise, nominal hover, one-motor-out hover, and steady climb. The cruise and nominal hover points determine the total energy consumption based on a simplified mission profile shown in Fig. 4. For static design optimization, we approximate the energy consumption of the takeoff, transition, and climb phase with the energy for 45 sec of hover [10]. The descent and landing phase is also approximated by an additional hover of 20 sec, assuming 1 m/s vertical descent for 20 m, which is double the no-fly zone (NFZ) height explained later in Sec. 5. Here, the UAV is assumed to glide down to 20 m altitude with zero power. We also assume that a UAV carries back the payload on the return flight, considering an undesirable scenario where the UAV cannot release the payload at the customer's location. In this case, the energy for a round trip is twice the energy for a one-way flight.

We use the one-motor-out hover condition to determine the lifting motor sizing and the steady climb condition to size the pusher, following the eVTOL conceptual design work [5]. To do so, we impose a power inequality constraint such that the lifting motor power rating must be higher than the power required at a one-motor-out steady hover. Likewise, we impose a pusher power constraint on the steady climb condition, where we set the 3 m/s rate of climb requirement [2]. The horizontal speed at the steady climb point is arbitrary and is an optimization variable. We also allow the UAV to use the lifting rotor to augment the lift in the climb condition.

4.2 Constraints

We set the maximum cruise lift coefficient of 0.8. We determined this value based on the cruise speed and wing area of the Wing's UAV, as shown in Table 2. The cruise speed variable is upper-bounded at 100 mph based on the FAA Part 107 requirement.

We also impose a geometry constraint to limit the lifting rotor radius. The rotor radius variable tends to reach the upper bound because a larger disk area lowers power consumption. The following geometry constraint prohibits interference between the lifting rotors and fuselage:

$$g(R, S) = 2R_{\text{lifter}} + 2d + w - \sqrt{S/AR} \leq 0 \ , \tag{9}$$

where d is the minimum separation between the fuselage and rotor tip and w is the fuselage width, and $AR = 6.6$ is the aspect ratio. We use $d = 0.05$ m from Ref. 2 and $w = 0.15$ m based on the Wing's UAV geometry [36]. In the chordwise direction, we assume that booms are long enough to separate the wing and rotors. On the pusher radius, we impose the upper bound of 0.3 m, which is double the baseline rotor radius. The upper bound of the rotor blade chord is 35% of the radius based on the small-scale propeller geometry data from the UIUC database [8, 35]

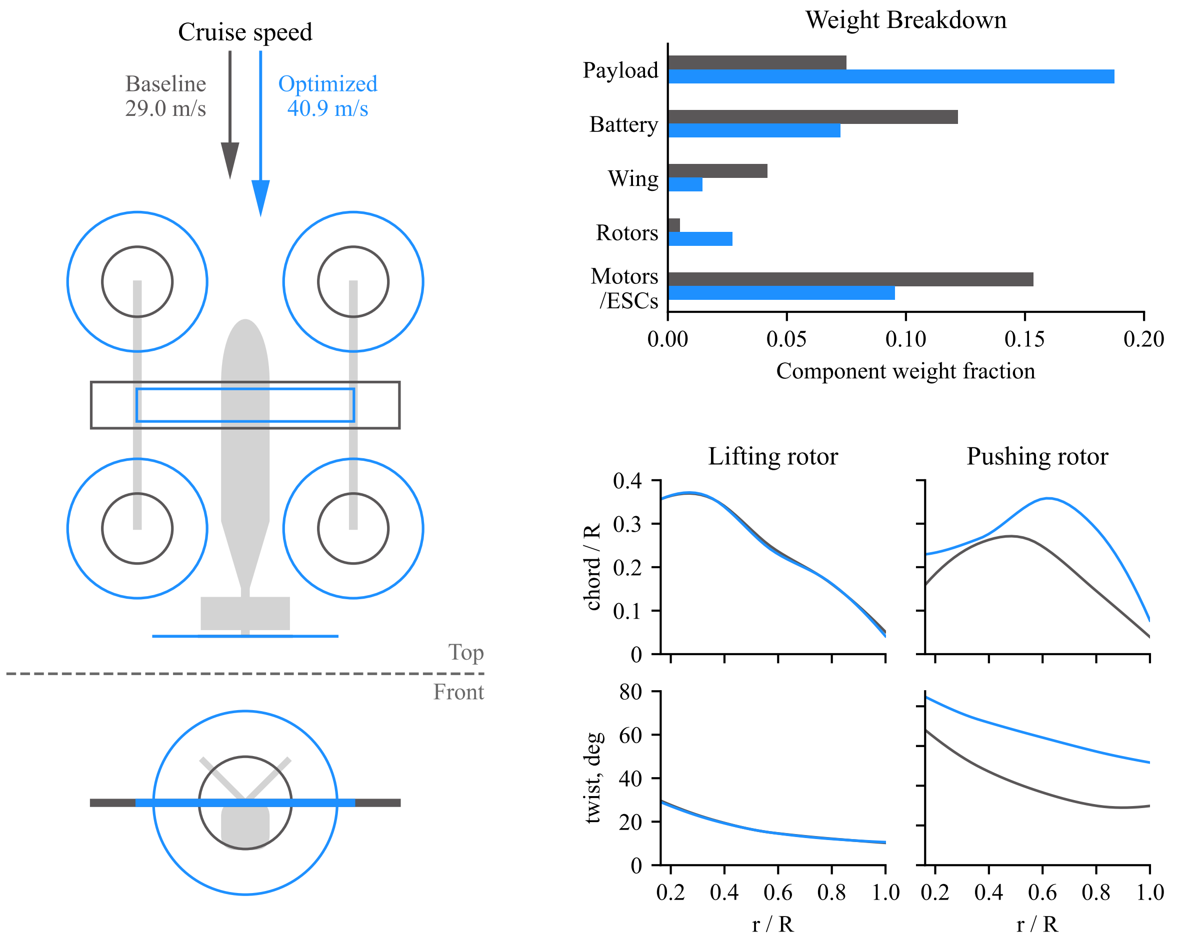

Figure 5: Comparison of the baseline UAV design and the statically-optimized design. The left figure shows the wing area, rotor radius, and cruise speed variables. The upper-right figure shows the component weight breakdown. The lower-right plots are the rotor blade designs.

4.3 Numerical Approach

We implemented the static design optimization problem using the OpenMDAO framework [40]. The derivatives are computed analytically, except for the BEM analysis that employs algorithmic differentiation. We use a sequential quadratic programming optimizer SNOPT [44] and pyOptSparse wrapper [45] for optimization. The optimization runtime was about 1 min on a desktop computer with a 3.4 GHz CPU.

4.4 Results

Figure 5 shows the static design optimization results. Here, we compare the optimized design to a baseline design based on the Wing's UAV. The baseline has the same cruise speed, wing area, and disk area as the Wing's vehicle. We then determined the baseline motor power ratings, rotor chord and twist, and the component weight breakdown by solving the static optimization problem while fixing the cruise speed, wing area, and disk area variables.

As a result of optimization, the payload weight increased by 0.72 kg compared to the baseline. The rotor radius became significantly larger to lower the disk loading. The geometry constraint limited the lifting rotor radius, and the pusher radius hit the upper bound. The lower disk loading reduced the power consumption, which ultimately decreased the battery, motors, and ESCs' weight. The larger rotor radius also increased the rotor weight, but overall, the weight reduction of the other components was more significant. The cruise speed also increased to reduce the wing area hence the wing weight. The higher cruise speed also shortened the cruise endurance. If we made the cruise speed even higher than the optimal value, the power required for the cruise would become too high.

The twist and normalized chord distribution of the lifting rotors were almost unchanged between the baseline and the optimized design because they are both optimized for the same hover condition. For the pushing rotor, the chord and twist increased compared to the baseline because the inflow conditions of the design point (i.e., cruise speed) has changed.

5 Takeoff Trajectory Optimization

Next, we minimize the energy consumption of the takeoff phase while fixing the UAV design. In this paper, "takeoff trajectory" means the vertical takeoff, climb to the cruise altitude, and acceleration to the cruise speed. Trajectory optimization determines the optimal flight path and control input history given the initial conditions (zero velocity on the ground) and the terminal conditions (cruise at 45 m altitude). The takeoff horizontal distance is assumed to be 1000 m in this section. For simultaneous design-trajectory optimization in Sec. 6, we also explore a 1500 m case and discuss the implication of the takeoff distance to the optimal UAV design and trajectory.

5.1 Boundary and Path Constraints

The initial and terminal conditions are:

$$\begin{aligned} x_0 &= 0 \ , \quad x_f = 1000 \ , \\ y_0 &= 0 \ , \quad y_0 = 45 \ , \\ v_{x_0} &= 0 \ , \quad v_{x_f} = v_{\text{cruise}} \ , \\ v_{y_0} &= 0 \ , \quad v_{y_f} = 0 \ , \\ \theta_0 &= 0 \ , \quad \theta_f = \theta_{\text{cruise}} \ . \end{aligned} \tag{10}$$

We impose the initial conditions by fixing the state variables at $t_0 = 0$. Terminal conditions are imposed as equality constraints.

We impose three path inequality constraints. First, the velocity cannot exceed 100 mph based on the FAA Part 107 requirement. Second, the power required must be lower than the motor power ratings (i.e., maximum steady power output), which was determined by the static design optimization. Third, we impose a vertical takeoff constraint to prohibit horizontal takeoff like a fixed-wing aircraft. For this purpose, we define an NFZ of 10 m height (typical height of a three-story building) with a 5 m horizontal radius from the takeoff point. Then, we require that one point along the trajectory, (x_v, y_v), must be within the 5 m radius and above the 10 m altitude threshold. The vertical takeoff requirement is illustrated in Fig. 6. This is not a rigorous NFZ path constraint, and a multimodal path (e.g., climb-dive-climb path) may violate the NFZ requirement while satisfying the above constraint. However, such a multimodal path is not energy-optimal; therefore, we do not consider these corner cases. The above constraint is equivalent to the NFZ path constraint for a monotonic climb.

The trajectory optimization problem is summarized in Table 4.

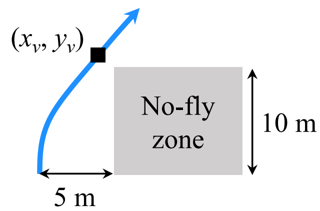

Figure 6: Schematic of the vertical takeoff requirement.

Table 4: Takeoff trajectory optimization problem.

		Function/variable	Description
minimize		E_f	energy consumption
by varying	time	t_f	duration
	states	x	horizontal location
		y	altitude
		v_x	horizontal speed
		v_y	vertical speed
		E	accumulated energy consumption
	controls	θ	body pitch attitude
		Ω_{lifter}	lifting rotor speed
		Ω_{pusher}	pushing rotor speed
subject to	terminal		Eq. (10) as equality constraints
	path	$P_{\text{lifter}} < \bar{P}_{\text{lifter}}$	lifting motor power upper bound
		$P_{\text{pusher}} < \bar{P}_{\text{pusher}}$	pushing motor power upper bound
		$v_x \leq 44.7$	PART 107 speed limit
		$x_v \leq 5,\ y_v \geq 10$	vertical takeoff requirement
	defect		to impose the equations of motion Eq. (1)

5.2 Numerical Approach

We use Dymos [46], an optimal control library built on top of the OpenMDAO framework. Dymos implements direct transcription methods to discretize a trajectory optimization problem and transcript it to a nonlinear optimization problem. In this work, we employed the third-order Radau collocation method [47] with 20 segments for the takeoff trajectory. The resulting problem has 507 optimization variables and 704 constraints whose Jacobian is sparse. We use the total Jacobian coloring[28, 40] to exploit the Jacobian sparsity and reduce the cost of computing derivatives.

We employed IPOPT [48] for trajectory optimization. The optimization runtime, including the coloring computation, was about 15 min without parallelization.

5.3 Results

Figure 7 shows the optimized takeoff trajectory. The red vectors visualize the thrust vector (lifter and pusher combined), and the airfoil profiles show the body pitch angle. The thrust vector and pitch angle were plotted at a 3-sec interval. The black vectors at the bottom are the flight velocity.

The blue line in Fig. 7 is the result of the original trajectory optimization problem stated in Table 4. The optimized trajectory was energy-inefficient, using the lifting rotors to gain altitude to 45 m and the pusher to accelerate to the cruise speed. The takeoff and climb phases consumed 23.954 Wh per round-trip, which accounts for 41.8% of the total energy consumption for the round-

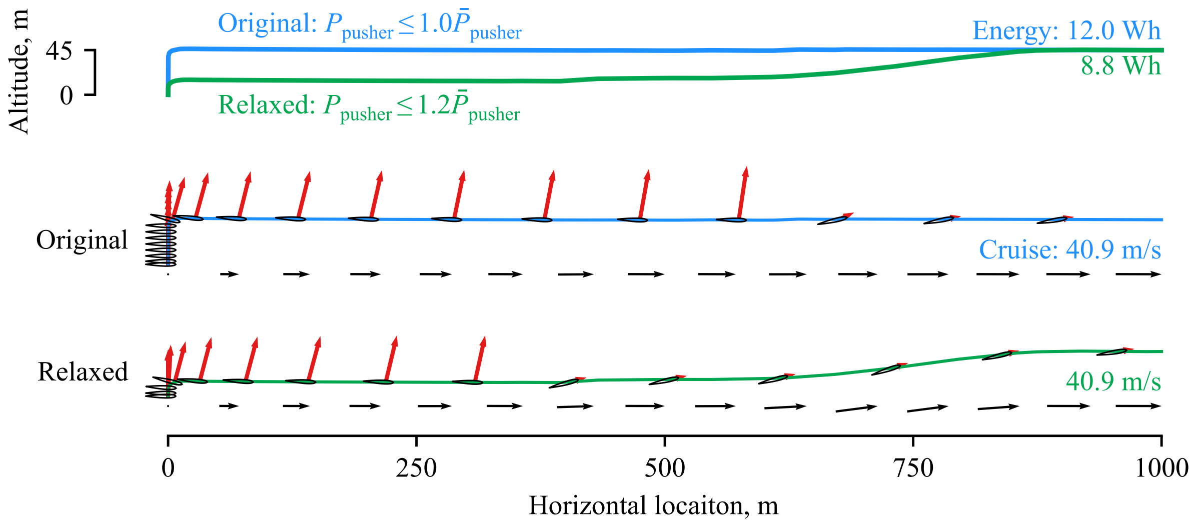

Figure 7: Optimized takeoff paths with a fixed UAV design. The red vectors, airfoil profiles, and black vectors show the thrust, body pitch angle, and flight velocity, respectively. The blue line is the original trajectory optimization result, whereas the green line relaxes the pusher power upper bound.

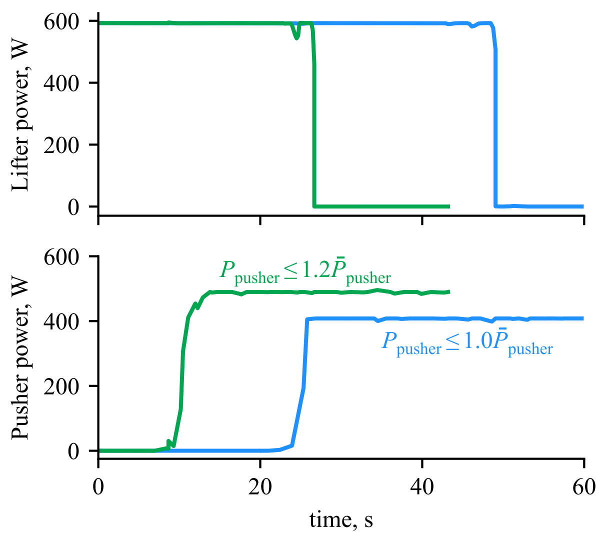

Figure 8: Power history of the lifting motors (top) and the pushing motor (bottom) for the fixed-design trajectory optimizations.

trip mission. The trajectory was limited by the power upper bound, which comes from the motor power rating determined in the UAV design optimization process. Figure 8 shows the power histories of the lifting and pushing motors. We see that the power histories hit the upper bounds. In particular, the pusher's power upper bound was the main factor for the energy-inefficient trajectory. The pushing motor was too weak to perform a wing-borne climb while accelerating to the cruise speed within the 1000 m distance. Consequently, the UAV had to use the lifting rotors to gain all the altitude first, then it accelerated without climbing.

Suppose we relax the pusher's power upper bound by setting $P \leq 1.2\bar{P}_{\text{pusher}}$. In that case, the UAV can climb using the wing (green line in Fig. 7). The takeoff energy consumption reduces to 17.631 Wh, which is 26.4% lower than the original trajectory. The lower energy consumption means a lower battery weight, which can increase the payload weight. However, increasing the power upper bound (which equals the motor power rating) results in a heavier motor, which decreases the payload capacity. We cannot know which of these—takeoff energy decrease or motor weight increase—is more significant if we optimize the UAV design and trajectory separately. This highlights the need for coupling trajectory optimization to the UAV conceptual design: simultaneous design-trajectory optimization can capture the above trade-off to find the best UAV design.

6 Simultaneous Design-Trajectory Optimization

Finally, we combine the design and trajectory optimization problems into a monolithic problem that simultaneously optimizes the UAV design and trajectory. Table 5 summarizes the optimization problem statement, and Fig. 10 visualizes the problem structure via the extended design structure matrix [49]. We maximize the payload weight with respect to the UAV conceptual design variables, the control inputs at the four steady points, and the takeoff trajectory. The simultaneous optimization problem includes all optimization variables and constraints from the static design optimization (Table 3) and the fixed-design trajectory optimization (Table 4). We still impose the pusher power constraint at the steady climb point to ensure a power margin for maneuverability, even though we now compute the takeoff and climb energy via trajectory optimization.

We use the mission profile shown in Fig. 9 to compute the energy required for a delivery mission. The mission consists of the takeoff, climb, and acceleration phases where the trajectory is optimized, steady cruise for 20 km round trip, steady hover for 30 sec, and descent and landing. We approximate the descent and landing phase by an additional hover for 20 sec, as we did for the static design optimization. Furthermore, we again assume that the UAV carries the payload back on the return flight in case it cannot release the payload.

6.1 Numerical Approach

We formulate design-trajectory optimization as a monolithic optimization problem. The numerical approach is similar to the fixed-design trajectory optimization, except we now have additional UAV design variables and constraints. The optimization problem has 533 variables and 715 constraints. We again use the Radau collocation method via Dymos and OpenMDAO.

Our approach is also called *direct transcription (DT) for co-design* [26] or *simultaneous formulation* [29]. In terms of the MDO architecture , the collocation method corresponds to the *simultaneous analysis and design* (SAND). Note that our approach is not rigorously SAND because we use a nonlinear solver to converge the BEM residuals at each time discretization point.

We used SNOPT for simultaneous optimization. We set the result from the static design optimization and fixed-design trajectory optimization as an initial guess to achieve fast and robust convergence. The runtime was about 17 min, including the time for total Jacobian coloring.

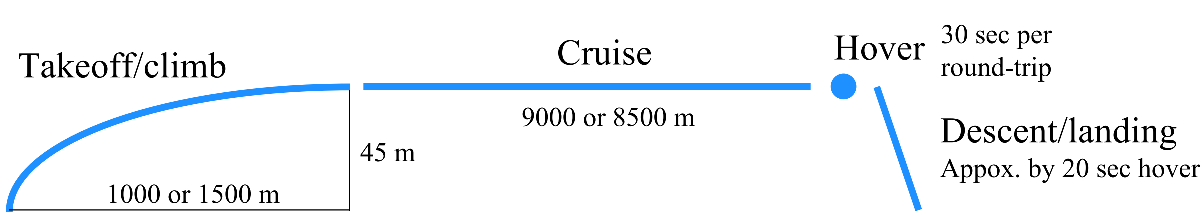

Figure 9: Mission profile used to compute the total energy consumption in simultaneous design-trajectory optimization. The figure only shows a one-way flight; in optimization, we compute the energy for a round-trip flight.

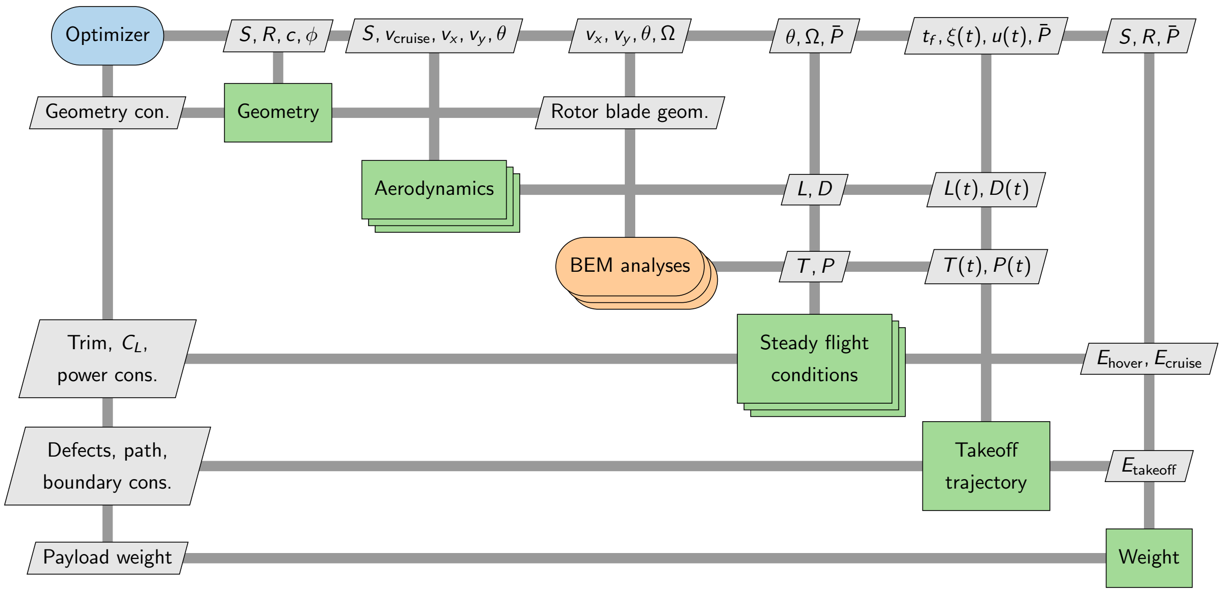

Figure 10: Problem structure of simultaneous design-trajectory optimization.

Table 5: Design-trajectory optimization problem.

maximize	payload weight	
by varying	UAV design	S, v_{cruise}
		$\bar{P}_{\text{lifter}}, \bar{P}_{\text{pusher}}$
		$R_{\text{lifter}}, R_{\text{pusher}}$
		$\phi_{\text{lifter}}, \phi_{\text{pusher}}$
		$c_{\text{lifter}}, c_{\text{pusher}}$
	steady control	v_x at steady climb point
		$\boldsymbol{u} := [\theta, \Omega_{\text{lifter}}, \Omega_{\text{pusher}}]$ at four steady points
	takeoff trajectory	t_f
		$\boldsymbol{u}(t)$
		$\boldsymbol{\xi}(t) := [x, y, v_x, v_y, E]$
subject to	all constraints in Tables 3 and 4	

6.2 Results with 1000 m Takeoff Distance

As a result of simultaneous optimization, we achieved a 5.3% increase in the payload weight compared to sequential optimization. Here, sequential optimization means one sequence of static design optimization followed by fixed-design trajectory optimization (without further iterations). Figure 11 shows the comparison of the vehicle design between the simultaneous and sequential optimizations. The sequentially-designed UAV has the same design as the static optimization result (Fig. 5) except for the battery and payload weight, which were recomputed using the takeoff energy consumption from the fixed-design optimization. Figure. 12 shows the takeoff flight paths of the sequential and simultaneous optimizations.

The simultaneous optimization reduced the cruise speed to 37.8 m/s from 40.9 m/s of the statically-optimized design. This increased the wing weight and cruise energy slightly, as shown in Fig. 11 and Table 6. However, as shown in Fig. 12, the UAV can now perform a wing-borne climb to reach the cruise speed because the lower cruise speed requires less acceleration. As a result of the energy-efficient wing-borne climb, the takeoff energy consumption was reduced by 41.8% compared

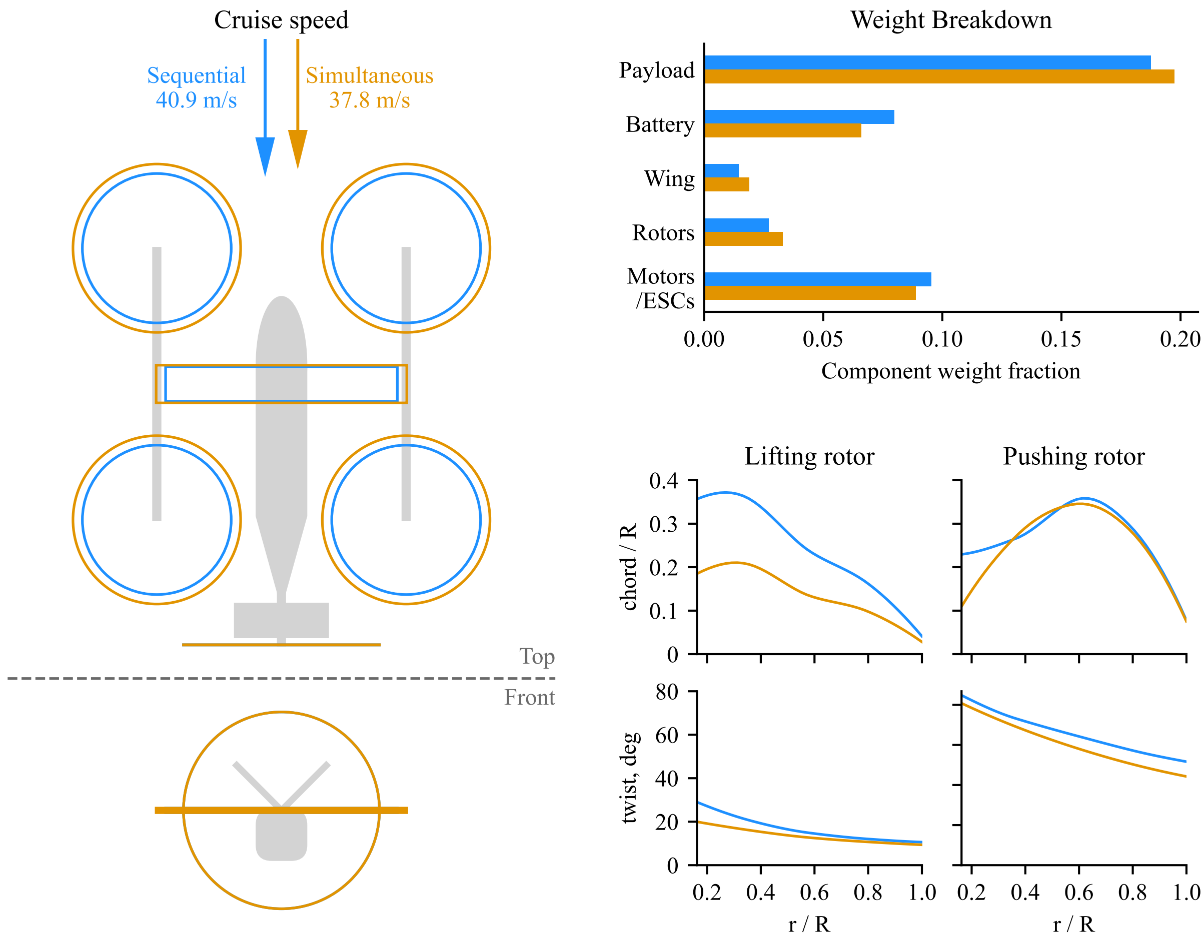

Figure 11: Comparison of the optimized UAV designs between the sequential and simultaneous optimizations (1000 m takeoff distance).

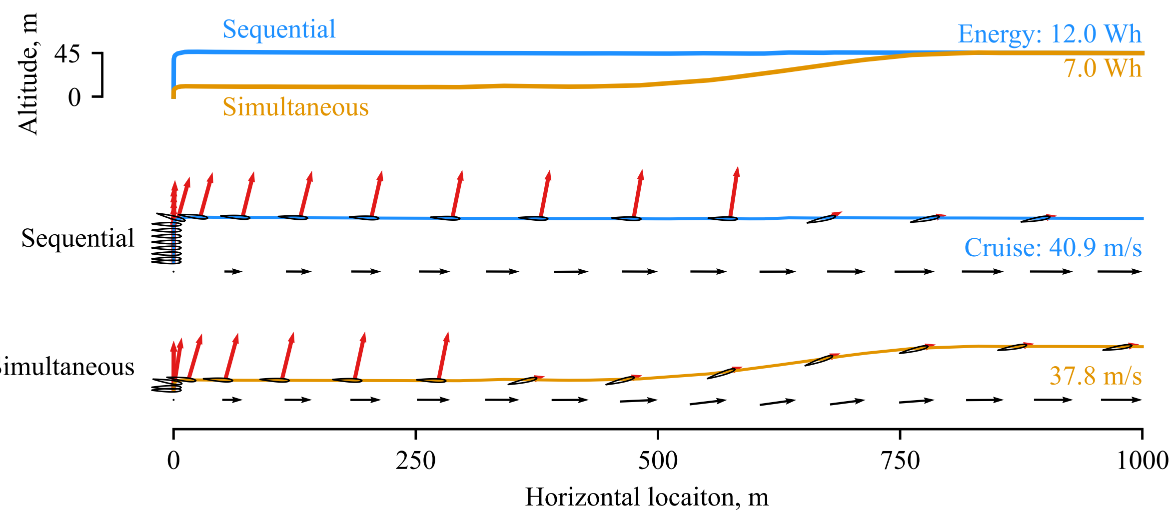

Figure 12: Comparison of takeoff paths between the sequential and simultaneous optimizations (1000 m takeoff distance).

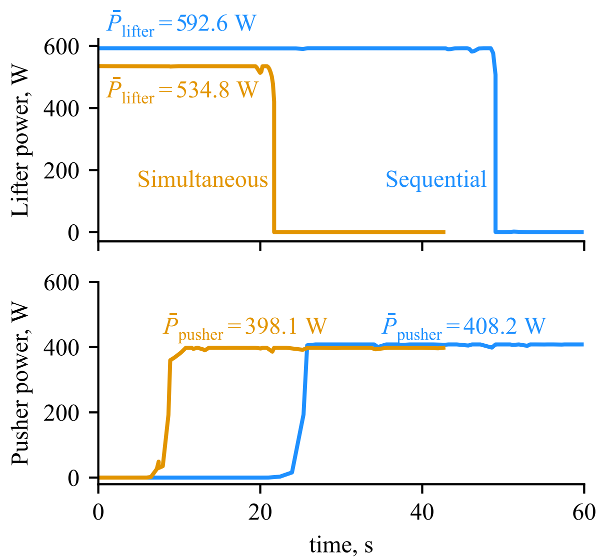

Figure 13: Comparison of power histories between the sequential and simultaneous optimizations (1000 m takeoff distance).

Table 6: Breakdown of energy consumption by phases for the 1000 m takeoff case (Wh, per round-trip).

	Total	Takeoff	Cruise	Hover	Landing
Sequential	57.237	23.954	23.295	4.281	5.708
Simultaneous	47.304	13.936	24.354	3.863	5.151

to the fixed-design trajectory. This significant decrease in the takeoff energy, hence the battery weight, was the main driver for the payload weight increase.

Furthermore, simultaneous optimization lowered the lifting motor power rating, as shown in Fig. 13. This also contributed to the payload weight increase by reducing the motor weight. The lower power rating was enabled by a larger disk area. The simultaneous solution had a larger wing area due to the lower cruise speed, and the larger wing area allowed a larger lifting rotor radius because it relaxed the geometry constraint Eq. (9).

On the lifting rotor blade, the normalized chord became shorter as a result of simultaneous optimization. The shorter blade chord reduced the lifting rotor power and in-plane force (which acts as additional drag) in the helicopter-like edgewise forward flight. To demonstrate this point, we performed a post-optimization BEM analysis of the lifting rotors at 20 m/s edgewise inflow (i.e., the inflow direction parallel to the rotor disk plane) and the rotor rotational speed equal to the hover condition. This setting represents helicopter-like acceleration, where the UAV uses rotors to generate lift instead of the wing during forward flight. Table 7 compares the ratio of the thrust to in-plane force T/F and the thrust-to-power ratio T/P between the sequential design and simultaneous design. Both ratios are higher with the simultaneous design, which indicates that the simultaneous design is more efficient in edgewise flight. On the other hand, the sequential design only considers hover and wing-borne forward flight conditions and does not consider the edgewise rotor-powered flight.

The pushing rotor's blade design did not change significantly. The simultaneous design has a slightly lower blade twist because the cruise speed decreased.

Table 7: Post-optimization BEM analysis results of the lifting rotors in edgewise forward flight.

	T/F	T/P (N/W)
Sequential	12.91	0.1227
Simultaneous	19.79	0.1362

6.3 Results with 1500 m Takeoff Distance

We also investigate the implication of the takeoff distance setting. In this section, we perform the same sequential and simultaneous optimizations but with a horizontal distance of 1500 m.

Figure 14 compares the takeoff trajectory between two optimizations. With a 1500 m distance, the sequential UAV design can also perform a wing-borne climb because it has enough distance to accelerate to the cruise speed while climbing, unlike the 1000 m takeoff case. Consequently, the difference between the sequential and simultaneous optimization results was smaller than the 1000 m case. We still achieved the payload weight increase by 2.4% with the simultaneous optimization compared to the sequential optimization.

The cruise speed of the simultaneous design was 39.9 m/s, slightly lower than the 40.9 m/s of the sequential design. Because of this, the UAV required less acceleration during the climb, which enabled an earlier shift to the wing-borne flight, as shown in Fig. 14. As a result, the takeoff energy consumption decreased by 20.8% compared to the sequential solution, as reported in The lower takeoff energy led to the battery weight reduction, which drove the payload weight increase. Table 8 summarizes the energy consumption by each phase.

Table 8: Breakdown of energy consumption by phases for the 1500 m takeoff case (Wh, per round-trip).

	Total	Takeoff	Cruise	Hover	Landing
Sequential	51.289	20.917	20.383	4.281	5.708
Simultanoues	47.226	16.572	20.910	4.177	5.569

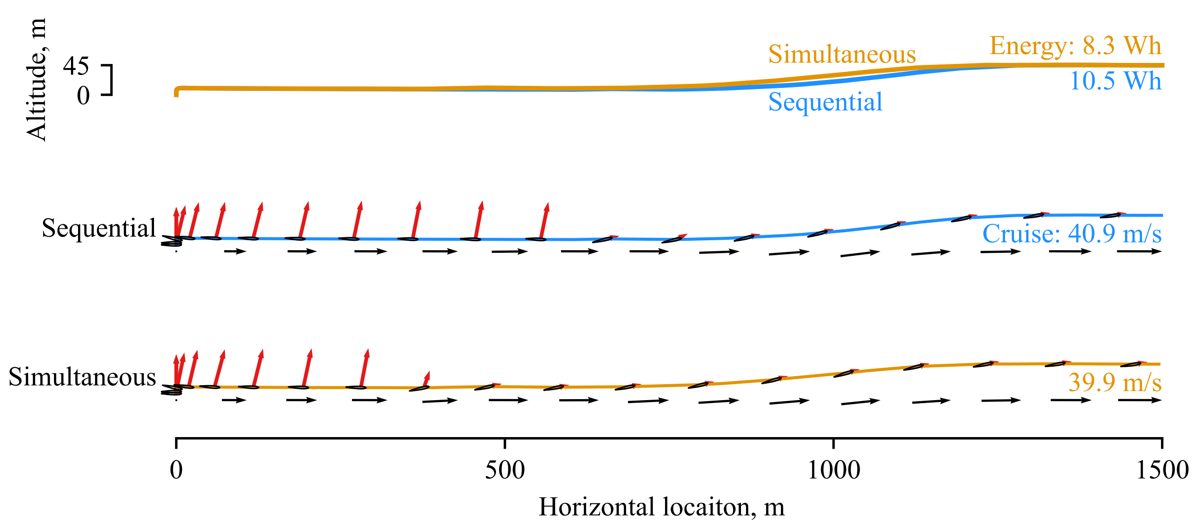

Figure 14: Comparison of takeoff paths between the sequential and simultaneous optimizations (1500 m takeoff distance).

7 Conclusions

In this work, we performed simultaneous optimization of the eVTOL UAV conceptual design and takeoff trajectory. In particular, we studied a lift-plus-cruise UAV for package delivery. Design-trajectory optimization allows us to find the optimal VTOL design that balances the efficiency between the vertical flight, takeoff transition, and cruise for maximum system-level performance.

First, we presented a conventional conceptual design optimization problem. We maximized the payload weight capacity given the mission requirements and the fixed takeoff weight. This problem evaluated four steady flight conditions (hover, cruise, one-motor-out hover, and wing-borne climb) to determine the optimal UAV design.

Next, we discussed takeoff trajectory optimization while fixing the UAV design. We used a direct collocation method with analytic derivatives and total Jacobian coloring to lower the computational cost. The resulting takeoff trajectory was energy-inefficient because the pusher motor power rating was too low and, it could not exploit the wing to climb efficiently. We then demonstrated that the takeoff energy consumption (hence the battery weight) could be significantly reduced if we increased the pusher power rating. However, the higher power rating also increases the motor weight. This trade-off between the motor sizing and takeoff energy consumption highlights the need for coupling trajectory optimization with the UAV conceptual design.

Finally, we performed the novel design-trajectory simultaneous optimization. The key findings are summarized as follows:

1. Design-trajectory optimization resulted in a 2.4–5.3% increase in the payload weight capacity compared to the conventional sequential optimization.
2. The cruise speed was reduced as a result of simultaneous optimization. Although the lower cruise speed slightly increased the cruise power consumption, it enabled an energy-efficient wing-borne climb because the UAV needs less acceleration to reach the cruise speed.
3. The pusher motor sizing significantly affected both UAV design and takeoff trajectory. The simultaneous optimization achieved optimal motor sizing, whereas the sequential optimization resulted in a suboptimal design.

Acknowledgments

This work was funded by Japan Student Services Organization (JASSO) Fellowship Program. The first author was also partially supported by the Michigan Institute for Computational Discovery and Engineering (MICDE) fellowship. The authors thank Max Opgenoord for giving feedback on this work. We also thank Daniel Ingraham for providing an example of the CCBlade's OpenMDAO wrapper.

References

[1] Stolaroff, J. K., Samaras, C., O'Neill, E. R., Lubers, A., Mitchell, A. S., and Ceperley, D., "Energy Use and Life Cycle Greenhouse Gas Emissions of Drones for Commercial Package Delivery," *Nature Communications*, Vol. 9, No. 409, 2018. doi:10.1038/s41467-017-02411-5.

[2] Tyan, M., Nguyen, N. V., Kim, S., and Lee, J.-W., "Comprehensive preliminary sizing/resizing method for a fixed wing – VTOL electric UAV," *Aerospace Science and Technology*, Vol. 71, 2017, pp. 30–41. doi:10.1016/j.ast.2017.09.008.

[3] Zhang, X., Xie, F., Ji, T., Zhu, Z., and Zheng, Y., "Multi-fidelity deep neural network surrogate model for aerodynamic shape optimization," *Computer Methods in Applied Mechanics and Engineering*, Vol. 373, 2021, p. 113485. doi:10.1016/j.cma.2020.113485.

[4] An, J.-H., Kwon, D.-Y., Jeon, K.-S., Tyan, M., and Lee, J.-W., "Advanced Sizing Methodology for a Multi-Mode eVTOL UAV Powered by a Hydrogen Fuel Cell and Battery," *Aerospace*, Vol. 9, No. 2, 2022. doi:10.3390/aerospace9020071.

[5] Chakraborty, I., and Mishra, A. A., "Sizing and Analysis of a Lift-Plus-Cruise Aircraft with Electrified Propulsion," *Journal of Aircraft*, Vol. 0, No. 0, 0, pp. 1–19. doi:10.2514/1.C037044.

[6] Bershadsky, D., Haviland, S., and Johnson, E. N., "Electric Multirotor Propulsion System Sizing for Performance Prediction and Design Optimization," *57th AIAA/ASCE/AHS/ASC Structures, Structural Dynamics, and Materials Conference*, 2016. doi:10.2514/6.2016-0581.

[7] Winslow, J., Hrishikeshavan, V., and Chopra, I., "Design Methodology for Small-Scale Unmanned Quadrotors," *Journal of Aircraft*, Vol. 55, No. 3, 2018, pp. 1062–1070. doi:10.2514/1.C034483.

[8] Vu, N. A., Dang, D. K., and Le Dinh, T., "Electric propulsion system sizing methodology for an agriculture multicopter," *Aerospace Science and Technology*, Vol. 90, 2019, pp. 314–326. doi:10.1016/j.ast.2019.04.044.

[9] Sridharan, A., Govindarajan, B., and Chopra, I., "A Scalability Study of the Multirotor Biplane Tailsitter Using Conceptual Sizing," *Journal of the American Helicopter Society*, Vol. 65, No. 1, 2020, pp. 1–18. doi:10.4050/JAHS.65.012009.

[10] Sridharan, A., and Govindarajan, B., "A Multidisciplinary Optimization Approach for Sizing Vertical Lift Aircraft," *Journal of the American Helicopter Society*, Vol. 67, No. 2, 2022, pp. 1–15. doi:10.4050/JAHS.67.022004.

[11] Govindarajan, B., and Sridharan, A., "Conceptual Sizing of Vertical Lift Package Delivery Platforms," *Journal of Aircraft*, Vol. 57, No. 6, 2020, pp. 1170–1188. doi:10.2514/1.C035805.

[12] Palaia, G., Abu Salem, K., Cipolla, V., Binante, V., and Zanetti, D., "A Conceptual Design Methodology for e-VTOL Aircraft for Urban Air Mobility," *Applied Sciences*, Vol. 11, No. 22, 2021. doi:10.3390/app112210815.

[13] Orndorff, N. C., and Hwang, J. T., "Investigation of Optimal Air-Taxi Transition Profiles using Direct-Transcription Trajectory Optimization," *AIAA AVIATION Forum*, 2022. doi:10.2514/6.2022-3485.

[14] Wang, M., Diepolder, J., Zhang, S., Söpper, M., and Holzapfel, F., "Trajectory optimization-based maneuverability assessment of eVTOL aircraft," *Aerospace Science and Technology*, Vol. 117, 2021, p. 106903. doi:10.1016/j.ast.2021.106903.

[15] Anderson, R., Willis, J., Johnson, J., Ning, A., and Beard, R. W., "A Comparison of Aerodynamics Models for Optimizing the Takeoff and Transition of a Bi-wing Tailsitter," *AIAA Scitech Forum*, 2021. doi:10.2514/6.2021-1008.

[16] Panish, L., and Bacic, M., "Transition Trajectory Optimization for a Tiltwing VTOL Aircraft with Leading-Edge Fluid Injection Active Flow Control," *AIAA Scitech Forum*, 2022. doi:10.2514/6.2022-1082.

[17] Delbecq, S., Budinger, M., Coic, C., and Bartoli, N., "Trajectory and design optimization of multirotor drones with system simulation," *AIAA Scitech Forum*, 2021. doi:10.2514/6.2021-0211.

[18] Chauhan, S. S., and Martins, J. R. R. A., "Tilt-wing eVTOL takeoff trajectory optimization," *Journal of Aircraft*, Vol. 57, No. 1, 2020, pp. 93–112. doi:10.2514/1.C035476.

[19] Pradeep, P., and Wei, P., "Energy Optimal Speed Profile for Arrival of Tandem Tilt-Wing eVTOL Aircraft with RTA Constraint," *Proceedings of IEEE/CSAA Guidance, Navigation and Control Conference (GNCC), Xiamen, China*, 2018. doi:10.1109/GNCC42960.2018.9018748.

[20] Verling, S., Stastny, T., Battig, G., Alexis, K., and Siegwart, R., "Model-based transition optimization for a VTOL tailsitter," *2017 IEEE International Conference on Robotics and Automation (ICRA)*, IEEE, 2017. doi:10.1109/icra.2017.7989454.

[21] Oosedo, A., Abiko, S., Konno, A., and Uchiyama, M., "Optimal transition from hovering to level-flight of a quadrotor tail-sitter UAV," *Autonomous Robots*, Vol. 41, No. 5, 2017, pp. 1143–1159. doi:10.1007/s10514-016-9599-4.

[22] Banazadeh, A., and Taymourtash, N., "Optimal Control of an Aerial Tail Sitter in Transition Flight Phases," *Journal of Aircraft*, Vol. 53, No. 4, 2016, pp. 914–921. doi:10.2514/1.C033339.

[23] Maqsood, A., and Go, T. H., "Optimization of transition maneuvers through aerodynamic vectoring," *Aerospace Science and Technology*, Vol. 23, No. 1, 2012, pp. 363–371. doi:10.1016/j.ast.2011.09.004.

[24] Kubo, D., and Suzuki, S., "Tail-Sitter Vertical Takeoff and Landing Unmanned Aerial Vehicle: Transitional Flight Analysis," *Journal of Aircraft*, Vol. 45, No. 1, 2008, pp. 292–297. doi:10.2514/1.30122.

[25] Garcia-Sanz, M., "Control Co-Design: An engineering game changer," *Advanced Control for Applications*, Vol. 1, No. 1, 2019, p. e18. doi:https://doi.org/10.1002/adc2.18.

[26] Allison, J. T., and Herber, D. R., "Multidisciplinary Design Optimization of Dynamic Engineering Systems," *AIAA Journal*, Vol. 52, No. 4, 2014, pp. 691–710. doi:10.2514/1.J052182.

[27] Martins, J. R. R. A., and Lambe, A. B., "Multidisciplinary Design Optimization: A Survey of Architectures," *AIAA Journal*, Vol. 51, No. 9, 2013, pp. 2049–2075. doi:10.2514/1.J051895.

[28] Martins, J. R. R. A., and Ning, A., *Engineering Design Optimization*, Cambridge University Press, Cambridge, UK, 2021. doi:10.1017/9781108980647, URL `https://mdobook.github.io`.

[29] Herber, D. R., and Allison, J. T., "Nested and Simultaneous Solution Strategies for General Combined Plant and Control Design Problems," *Journal of Mechanical Design*, Vol. 141, No. 1, 2018. doi:10.1115/1.4040705.

[30] Matos, N. M. B., and Marta, A. C., "Concurrent Trajectory Optimization and Aircraft Design for the Air Cargo Challenge Competition," *Aerospace*, Vol. 9, No. 7, 2022. doi:10.3390/aerospace9070378.

[31] Lupp, C. A., Clark, D. L., Aksland, C. T., and Alleyne, A. G., "Mission and Shape Optimization of a HALE Aircraft including Transient Power and Thermal Constraints," *AIAA AVIATION Forum*, 2022. doi:10.2514/6.2022-3935.

[32] Morita, N., Tsuchiya, T., and Taguchi, H., "MDO of Hypersonic Waverider with Trajectory-Aero-Structure Coupling," *23rd AIAA International Space Planes and Hypersonic Systems and Technologies Conference*, 2020. doi:10.2514/6.2020-2402.

[33] Balesdent, M., Brevault, L., Valderrama-Zapata, J.-L., and Urbano, A., "All-At-Once formulation integrating pseudo-spectral optimal control for launch vehicle design and uncertainty quantification," *Acta Astronautica*, Vol. 200, 2022, pp. 462–477. doi:https://doi.org/10.1016/j.actaastro.2022.08.032.

[34] Bacchini, A., Cestino, E., Van Magill, B., and Verstraete, D., "Impact of lift propeller drag on the performance of eVTOL lift+cruise aircraft," *Aerospace Science and Technology*, Vol. 109, 2021, p. 106429. doi:10.1016/j.ast.2020.106429.

[35] Brandt, J. B., Deters, R. W., Ananda, G. K., Dantsker, O. D., and Selig, M. S., "UIUC Propeller Database," , 2022. URL `https://m-selig.ae.illinois.edu/props/propDB.html`, retrieved December 15, 2022.

[36] Wing Aviation LLC, "How it works – Wing," , 2022. URL `https://wing.com/how-it-works/`, retrieved December 15, 2022.

[37] Tangler, J. L., and Ostowari, C., "Horizontal axis wind turbine post stall airfoil characteristics synthesization," Conference paper presented at the DOE/NASA Wind Turbine Technology Workshop, May 1984. In Collected Papers on Wind Turbine Technology, NASA-CR-195432, May 1995.

[38] Drela, M., "XFOIL: An Analysis and Design System for Low Reynolds Number Airfoils," *Low Reynolds Number Aerodynamics*, edited by T. J. Mueller, Springer Berlin Heidelberg, Berlin, Heidelberg, 1989, pp. 1–12. doi:10.1007/978-3-642-84010-4_1.

[39] Ning, A., "Using blade element momentum methods with gradient-based design optimization," *Structural and Multidisciplinary Optimization*, 2021. doi:10.1007/s00158-021-02883-6.

[40] Gray, J. S., Hwang, J. T., Martins, J. R. R. A., Moore, K. T., and Naylor, B. A., "OpenMDAO: An open-source framework for multidisciplinary design, analysis, and optimization," *Structural and Multidisciplinary Optimization*, Vol. 59, No. 4, 2019, pp. 1075–1104. doi:10.1007/s00158-019-02211-z.

[41] McVeigh, M., "The V-22 tilt-rotor large-scale rotor performance/wing download test and comparison with theory," *Vertica*, Vol. 10, No. 3, 1986, pp. 281–297.

[42] Kaneko, S., and Martins, J. R. R. A., "Fleet Design Optimization of Package Delivery UAVs Considering Operations," *AIAA SciTech Forum*, 2022. doi:10.2514/6.2022-1503.

[43] Ma, Y., Zhang, W., Zhang, Y., Zhang, X., and Zhong, Y., "Sizing Method and Sensitivity Analysis for Distributed Electric Propulsion Aircraft," *Journal of Aircraft*, Vol. 57, No. 4, 2020, pp. 730–741. doi:10.2514/1.C035581.

[44] Gill, P. E., Murray, W., and Saunders, M. A., "SNOPT: An SQP Algorithm for Large-Scale Constrained Optimization," *SIAM Review*, Vol. 47, No. 1, 2005, pp. 99–131. doi:10.1137/S0036144504446096.

[45] Wu, N., Kenway, G., Mader, C. A., Jasa, J., and Martins, J. R. R. A., "pyOptSparse: A Python framework for large-scale constrained nonlinear optimization of sparse systems," *Journal of Open Source Software*, Vol. 5, No. 54, 2020, p. 2564. doi:10.21105/joss.02564.

[46] Falck, R., Gray, J. S., Ponnapalli, K., and Wright, T., "dymos: A Python package for optimal control of multidisciplinary systems," *Journal of Open Source Software*, Vol. 6, No. 59, 2021, p. 2809. doi:10.21105/joss.02809.

[47] Garg, D., Patterson, M., Darby, C., Francolin, C., Huntington, G., Hager, W., and Rao, A., "Direct Trajectory Optimization and Costate Estimation of General Optimal Control Problems Using a Radau Pseudospectral Method," *AIAA Guidance, Navigation, and Control Conference*, 2009. doi:10.2514/6.2009-5989.

[48] Curtis, F. E., Schenk, O., and Wächter, A., "An Interior Point Algorithm for Large-Scale Nonlinear Optimization with Inexact Step Computations," *SIAM Journal on Scientific Computing*, Vol. 32, No. 6, 2010, pp. 3447–3475.

[49] Lambe, A. B., and Martins, J. R. R. A., "Extensions to the Design Structure Matrix for the Description of Multidisciplinary Design, Analysis, and Optimization Processes," *Structural and Multidisciplinary Optimization*, Vol. 46, No. 2, 2012, pp. 273–284. doi:10.1007/s00158-012-0763-y.